

# A pan-cancer deep learning platform for prognostic prediction of metastatic progression and site tropism from primary tumor histopathology

Yixin Chen<sup>1†</sup>, Ziyu Su<sup>1†</sup>, Lingbin Meng<sup>3</sup>, Elshad Hasanov<sup>3</sup>,  
Wei Chen<sup>2</sup>, Anil Parwani<sup>2</sup>, M. Khalid Khan Niazi<sup>1,2\*</sup>

<sup>1</sup>Department of Biomedical Engineering, The Ohio State University, Columbus, OH, USA.

<sup>2</sup>Department of Pathology, College of Medicine, The Ohio State University Wexner Medical Center, Columbus, OH, USA.

<sup>3</sup>Department of Internal Medicine, Division of Medical Oncology, The Ohio State University Wexner Medical Center, Columbus, OH, USA.

\*Corresponding author(s). E-mail(s): [Khalid.Niazi@osumc.edu](mailto:Khalid.Niazi@osumc.edu);  
Contributing authors: [che395@osumc.edu](mailto:che395@osumc.edu); [Ziyu.Su@osumc.edu](mailto:Ziyu.Su@osumc.edu);  
[Lingbin.Meng@osumc.edu](mailto:Lingbin.Meng@osumc.edu); [Elshad.Hasanov@osumc.edu](mailto:Elshad.Hasanov@osumc.edu);  
[Wei.Chen@osumc.edu](mailto:Wei.Chen@osumc.edu); [Anil.Parwani@osumc.edu](mailto:Anil.Parwani@osumc.edu);

†The authors contributed equally to this work. The names are mentioned in alphabetical order.

## Abstract

Metastatic Progression remains the leading cause of cancer-related mortality, yet predicting whether a primary tumor will metastasize and where it will disseminate directly from histopathology remains a fundamental challenge. Although whole-slide images (WSIs) provide rich morphological information, prior computational pathology approaches typically address metastatic status or site prediction as isolated tasks, and do not explicitly model the clinically sequential decision process of metastatic risk assessment followed by downstream site-specific evaluation. To address this research gap, we present a decision-aware, concept-aligned MIL framework, HistoMet, for prognostic metastatic outcome prediction from primary tumor WSIs. Our proposed framework adopts a two-module prediction pipeline in which the likelihood of metastatic progression from the primary tumor is first estimated, followed by conditional prediction of metastatic site for high-risk cases. To guide representation learning and improve

clinical interpretability, our framework integrates linguistically defined and data-adaptive metastatic concepts through a pre-trained pathology vision-language model. We evaluate HistoMet on multi-institutional pan-cancer cohort of 6504 patients with metastasis follow-up and site annotations. Under clinically relevant high-sensitivity screening settings (95% sensitivity), HistoMet significantly reduces downstream workload while maintaining high metastatic risk recall. Conditional on metastatic cases, HistoMet achieves a macro-F1 of  $74.6 \pm 1.3$  and a macro one-vs-rest AUC of  $92.1 \pm 0.9$  for metastatic site prediction, outperforming state-of-the-art (SOTA) baselines. These results demonstrate that explicitly modeling clinical decision structure enables robust and deployable prognostic prediction of metastatic progression and site tropism directly from primary tumor histopathology.

## 1 Introduction

Computational Pathology (CPath) enables quantitative analysis of digitized histopathology images and plays a crucial role in cancer prognosis. Despite its clinical importance, prognostic assessment based on primary tumor histology still depends heavily on manual interpretation by pathologists, making the process time-consuming and difficult to scale in routine clinical practice [1, 2]. Achieving precise and reliable prognostic stratification at the time of primary tumor diagnosis is essential for guiding treatment decisions, including the choice of adjuvant therapies, appropriate surveillance, and follow-up strategies [3–5]. However, current prognostic tools—such as histologic grading and molecular assays [6]—face limitations related to computational cost, tissue requirements, and universal accessibility. Importantly, the direct prediction of a primary tumor’s metastatic potential from tumor morphology remains largely uninvestigated, even though this task is critical for enabling earlier risk stratification and more personalized clinical management.

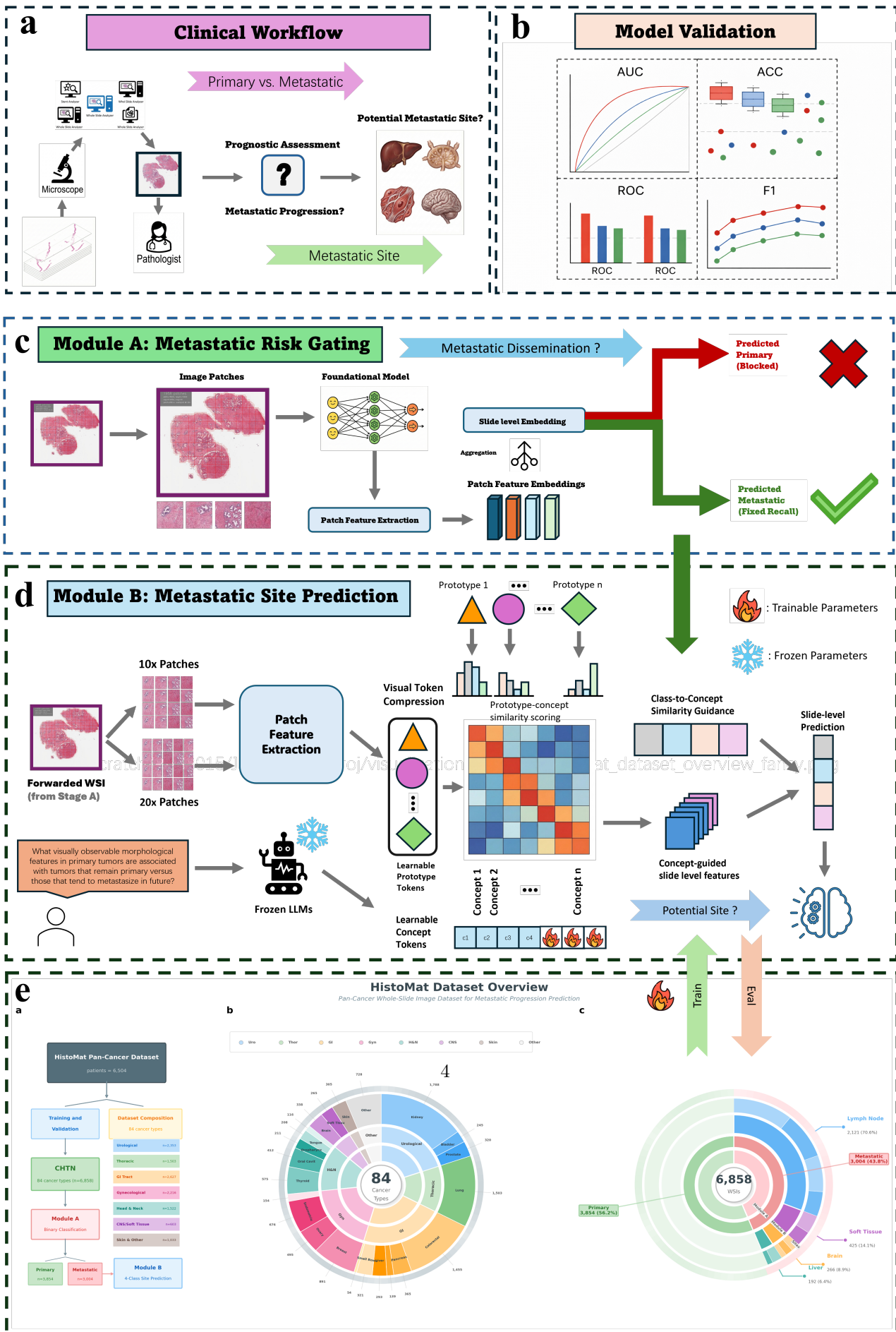
The digitization of histopathology slides into high-resolution whole-slide images (WSIs) has facilitated the development of computer-aided methods for large-scale prognostic analysis [3, 7, 8]. Due to the lack of fine-grained annotations and the substantial size of WSIs, Multiple Instance Learning (MIL) [9–11] has emerged as a prevalent framework for WSI analysis under weak supervision. In MIL, WSIs are represented as collections of patch-level feature embeddings extracted using pre-trained models, which are then aggregated to generate slide-level representations for prediction. Most current computational approaches, however, rely on single-step, image-driven feature aggregation. These methods often fail to capture the explicit sequential reasoning and high-level clinical concepts that clinicians employ when assessing disease progression from primary tumors. Consequently, relying solely on visual features limits the interpretability of prognostic profiling, highlighting a critical need to integrate clinically meaningful semantic knowledge into the modeling process.

To address this semantic gap, the rapid development of multimodal learning has spurred growing interest in vision-language models (VLMs) within computational

pathology. CLIP-based [12–15] pathology vision–language models learn aligned representation spaces between histopathology images and natural language descriptions, enabling the grounding of visual patterns in textual concepts. While recent research has investigated the integration of such language-based guidance [16–19] into WSI analysis, these studies have primarily addressed zero-shot, few-shot, or weakly supervised scenarios—typically for diagnostic tasks like classification and retrieval. As a result, the potential of VLMs to enhance fully supervised prognostic modeling—by explicitly modeling disease progression through rich semantic structures—remains a promising but largely unexplored avenue.

To address the limitation where most existing pathology vision–language models have primarily been explored for diagnostic tasks [20–22]—such as classification, segmentation, and retrieval—rather than for downstream prognostic modeling, we present HistoMet, a two-module concept-aligned prognostic framework that predicts the likelihood of metastatic progression and the potential metastatic site using only primary slides. Building on prior research demonstrating that histopathologic morphology encodes clinically meaningful phenotypic signals reflective of underlying tumor biology [23, 24], HistoMet is among the first frameworks to explicitly siteize primary tumor morphological cues into a prognostic task for predicting metastatic progression and metastatic site tropism. Rather than treating prognosis as a monolithic prediction, HistoMet decomposes the task into two modules: the first determines the trajectory of progression (localized vs. metastatic), which then conditions the second module to predict the specific potential site of metastasis. To further enhance interpretability, HistoMet integrates learnable site-tropism phenotype-related concepts through a pre-trained pathology vision language model [25]. Finally, instead of relying on opaque feature extraction, the framework aligns condensed visual prototype tokens with morphological and cancer-type-agnostic semantic entities encoded by frozen LLMs at 10 $\times$  and 20 $\times$  magnifications, generating concept-enhanced slide-level features for interpretable metastatic site prediction in a fully supervised setting.

We validated our proposed framework based on three complementary downstream tasks: (a) primary versus metastatic binary classification task (b) conditional prediction of metastatic site tropism among cases predicted to progress (c) end-to-end two-stage prediction under high-sensitivity operating point [26–28]. This work represents one of the first attempts to frame metastases prediction as a prognostic task based on primary tumor histology. HistoMet outperforms all previous SOTA MIL baselines across all evaluations.



- a.** Clinical motivation and task formulation for prognostic prediction of metastatic progression and site tropism from primary tumor whole-slide images.
- b.** Two-stage decision-aware framework in which Module A performs high-sensitivity metastatic risk screening and Module B conditionally predicts metastatic site among high-risk cases.
- c.** Module A aggregates multi-scale (10 $\times$  and 20 $\times$ ) patch features to produce slide-level predictions that gate downstream analysis under fixed high-sensitivity operating points.
- d.** Module B condenses patch-level features into learnable visual prototypes and aligns them with semantic morphology concepts for metastatic site prediction.
- e.** Concept-guided multi-scale fusion, dataset overview, and evaluation protocol used to assess progression prediction, conditional site prediction, and end-to-end system performance.

## 2 Results

### 2.1 Dataset characteristics for tumor prognosis

We evaluate HistoMet on a cohort of primary tumor whole-slide images (WSIs) curated for prognostic prediction of metastases. The dataset contains 6504 patients represented by 6858 WSIs with detailed pathology reports, and the complete dataset statistics are shown in Fig. 1. All samples are derived primarily from primary tumors, and these samples are used for training for both stages. For the prognostic metastasis progression task, in stage one, 3004 cases developed metastases during follow-up, while 3854 slides showed no metastatic progression. Metastatic status is a critical determinant of treatment planning. However, existing approaches to assess the risk of metastatic progression include molecular profiling and longitudinal image surveillance 23–25, which are highly time-consuming and labor-intensive in resource-constrained clinical settings. Additionally, this approach might not capture heterogeneous morphological visual cues indicative of metastatic progression in H&E slides. For patients predicted to develop metastasis, we further evaluate site tropism in stage two. In our dataset, the metastatic sites include the brain, lymph nodes, liver, and soft tissue, with class counts of 266, 2121, 192, and 425, respectively. Our dataset is highly imbalanced for the metastatic site, which mimics the real-world clinical setting. Typical assessment of site-specific metastatic progression includes downstream imaging or molecular inspection26. Prior studies18,19 demonstrate that gene and molecular expression patterns are reflective of metastatic potential and site tropism. However, only a few of them investigate pan-cancer site metastasis. Therefore, we hypothesize that certain morphological phenotypes will be indicative of metastatic site prediction. For the evaluation of module one, module two, and the end-to-end stage, we use the area under the receiver operating characteristic curve (AUC) and accuracy (ACC) as evaluation metrics. For each module, we perform a 5-fold cross-validation and report the results of all models using mean value and standard deviations. Additionally, HistoMet could operate on different pathology foundational models, and we utilize Conch [14] as the feature extractor for HistoMet and other baselines.

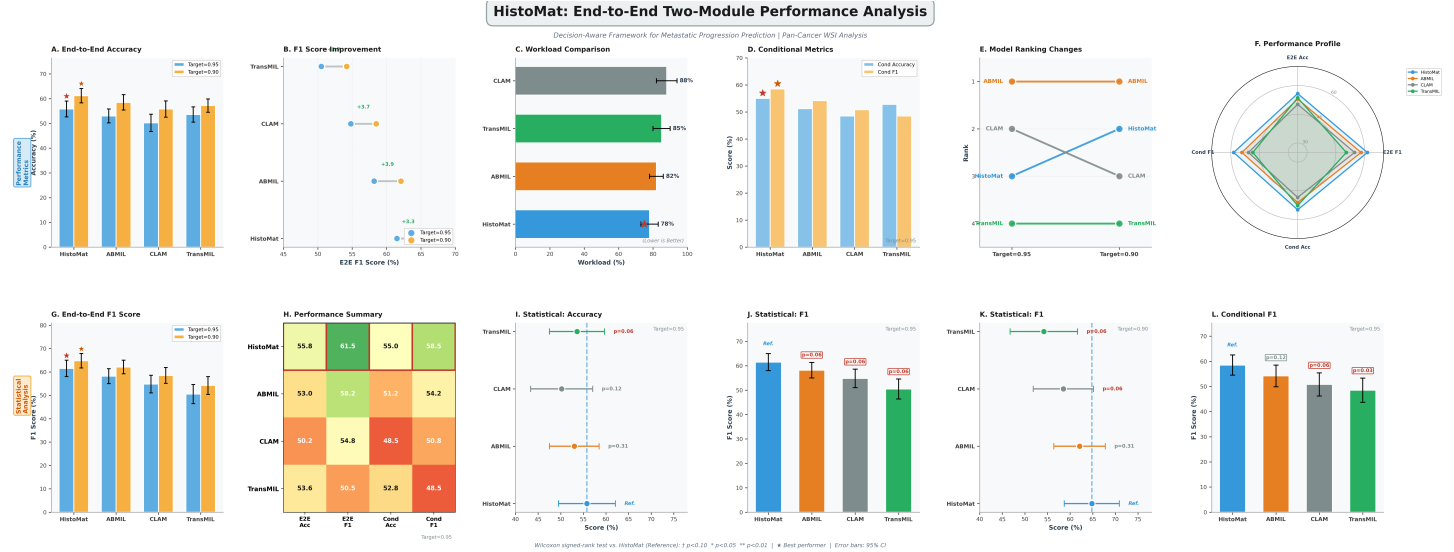


**Fig. 2: End-to-end performance evaluation of the HistoMet two-module framework for metastatic progression prediction.** **A.** End-to-end accuracy comparison across four models (HistoMet, ABMIL, CLAM, TransMIL) at two operating points (Target Sensitivity = 0.95 and 0.90). **B.** Dumbbell plot showing E2E F1 score changes when relaxing target sensitivity from 0.95 to 0.90. **C.** Workload comparison indicating the proportion of cases requiring expert review. **D.** Conditional site prediction metrics for Module B, evaluated only on cases correctly identified as metastatic by Module A. **E.** Bump chart illustrating model ranking changes across operating points. **F.** Radar plot summarizing multi-metric profiles across E2E and conditional metrics. **G.** End-to-end F1 score comparison against baseline methods. **H.** Performance summary heatmap with best performers highlighted. **I.** Forest plot with 95% confidence intervals for E2E accuracy at each sensitivity threshold. **J.** Statistical comparison of F1 scores with significance annotations. **K.** Forest plot with 95% confidence intervals for E2E F1 at each sensitivity threshold. **L.** Statistical comparison of accuracy scores with significance annotations.

## 2.2 HistoMet helps in prognostic decision

For evaluation, we compared the performance of HistoMet against several state-of-the-art (SOTA) methodologies: (1) ABMIL, (2) TransMIL, (3) CLAM. We show that HistoMet surpasses all the baselines in across the metastatic progression (Module A) and metastatic site (Module B) downstream tasks. At clinically relevant high-sensitivity operating points for metastasis prediction, HistoMet achieved substantially improved specificity relative to the best-performing baselines at a fixed sensitivity of 95% for Module A. For Module B, HistoMet yields higher macro-F1 scores across rare potential metastatic sites, demonstrating that adding semantic-language priors based on primary tumor morphology significantly enhances site tropism. The downstream task we address in this study involves complex inference from primary tumor histology, requiring the integration of morphological cues across heterogeneous spatial scales. Rather than performing direct classification of metastatic tissue or relying on cancer type-specific histologic patterns, our proposed framework is cancer type-agnostic and can infer metastasis based on common and weakly expressed morphological cues associated with the primary tumor. From the observed performance, we deduce that

explicitly modeling sequential reasoning with efficient integration of multi-scale fusion, visual information aggregation, and semantic language guidance is essential for solving these two downstream tasks. Overall, HistoMet demonstrates its ability to predict metastatic progression potential and possible metastatic locations, supporting its potential utility for decision-aware metastasis prediction.

### 2.3 Decision-Aware end-to-end performance under High-Sensitivity Operating Points

We evaluated the proposed two-module pipeline under fixed high-sensitivity operating points to simulate clinical deployment scenarios. For each target sensitivity (0.95 and 0.90), a decision threshold for Module A metastatic screening was selected on the validation set and subsequently applied to the test cohort. The entire pipeline is treated as an end-to-end system that outputs one of five classes (Primary or one of four metastatic sites) under this decision-aware evaluation setting. Therefore, end-to-end evaluation explicitly accounts for error propagation, including false positives of primary cases, missed metastatic cases blocked by Module A, and incorrect site predictions by Module B.

At a target sensitivity of 0.95, HistoMet achieved an end-to-end 5-class accuracy of 55.76% and a macro-F1 of 61.22%, outperforming CLAM and TransMIL while remaining competitive with ABMIL. Notably, despite similar Module A sensitivities across methods, substantial differences were observed in end-to-end macro-F1, highlighting that system-level performance is strongly influenced by the structure of propagated errors rather than screening sensitivity alone. When the target sensitivity was set to 0.90, the improved specificity reduced the redundant computational cost incurred, and all methods demonstrated consistent improvements under this relaxed operating point. HistoMet demonstrates the most stable macro-F1 under both clinical operating points.

Notably, the observed performance gaps between models are mainly caused by amplification of upstream error propagation. Under high-sensitivity screening, false positives from Module A and false negatives from Module A will degrade end-to-end performance, particularly for rare metastatic sites. For example, macro-F1 for some competing methods downgrades due to unstable error distributions, even when overall accuracy remains comparable. These results demonstrate the need for decision-aware end-to-end evaluation.

### 2.4 Effectiveness of Module A for Metastasis Prediction

The metastasis prediction (Module A) aims to perform prediction of metastatic risk based on pan-cancer primary tumor slides. We first evaluate its performance as a reliable prognostic metastatic risk classifier, which is used to distinguish primary cases that will subsequently develop distant metastasis. Based on experimental results, Module A consistently outperforms competing baselines, demonstrating strong overall discrimination for metastatic risk prediction. Beyond overall classification ability, the primary clinical role of Module A is to function as a screening gate for prognostic

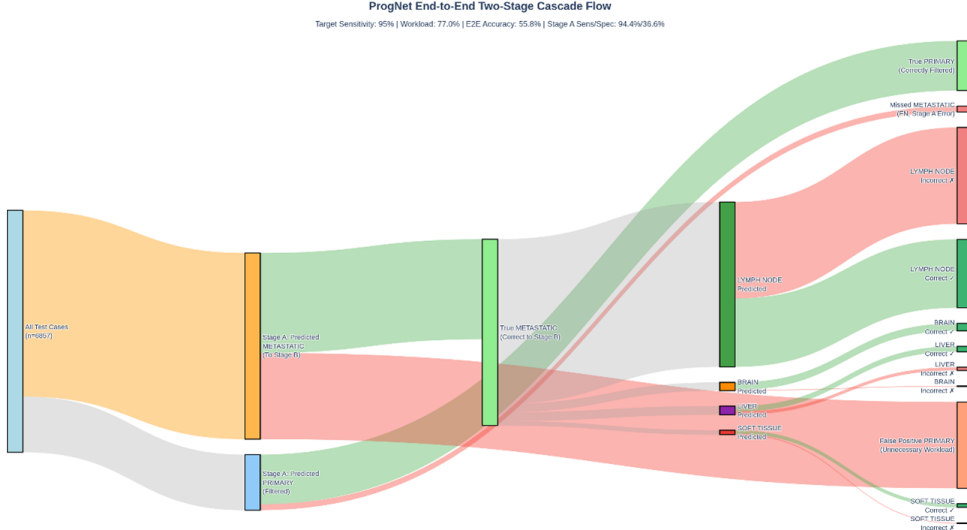


**Fig. 3: Comprehensive evaluation of Module A binary screening performance.** The Sankey diagram illustrates patient-level case flow from initial binary screening (Module A) to final 5-class prediction across the full test cohort ( $n = 6,857$ ). Module A filters 23.0% of cases as predicted primary tumors, while 77.0% are forwarded to Module B for metastatic site prediction. Among filtered cases, 1,409 are correctly identified as primary tumors (true negatives), whereas 168 metastatic cases are missed (false negatives). Cases forwarded to Module B include 2,836 true metastatic cases (true positives) and 2,444 false-positive primary cases, representing unnecessary workload. Module B performs 4-class metastatic site prediction (lymph node, soft tissue, brain, liver). Overall, the system achieves 55.75% end-to-end 5-class accuracy with a 23.0% workload reduction compared to processing all cases. Flow width is proportional to case count; green and red flows denote correct and incorrect decisions, respectively.

metastatic prediction, where minimizing missed metastatic cases are critical. Accordingly, we assess metastatic prediction (Module A) performance under high-sensitivity clinical operating points that explicitly prioritize sensitivity for detecting metastatic cases. Under this setting, sensitivity is fixed to capture the majority future metastatic cases, and specificity is used to quantify the model's ability to correctly eliminate low-risk primary cases and thereby reduce redundant downstream analysis.

We evaluate Module A under clinically relevant high-sensitivity operating points to assess its role as a prognostic screening gate, where minimizing missed metastatic cases is critical. As shown in Fig. 4, HistoMet consistently achieves higher specificity than competing baselines at matched sensitivity levels, resulting in fewer missed metastatic cases and reduced unnecessary downstream analysis. These improvements are particularly evident at the sensitivity levels commonly adopted in clinical screening scenarios (e.g., 90% and 95%), highlighting HistoMet's ability to balance sensitivity and specificity under screening constraints. In addition, the calibration analysis shown

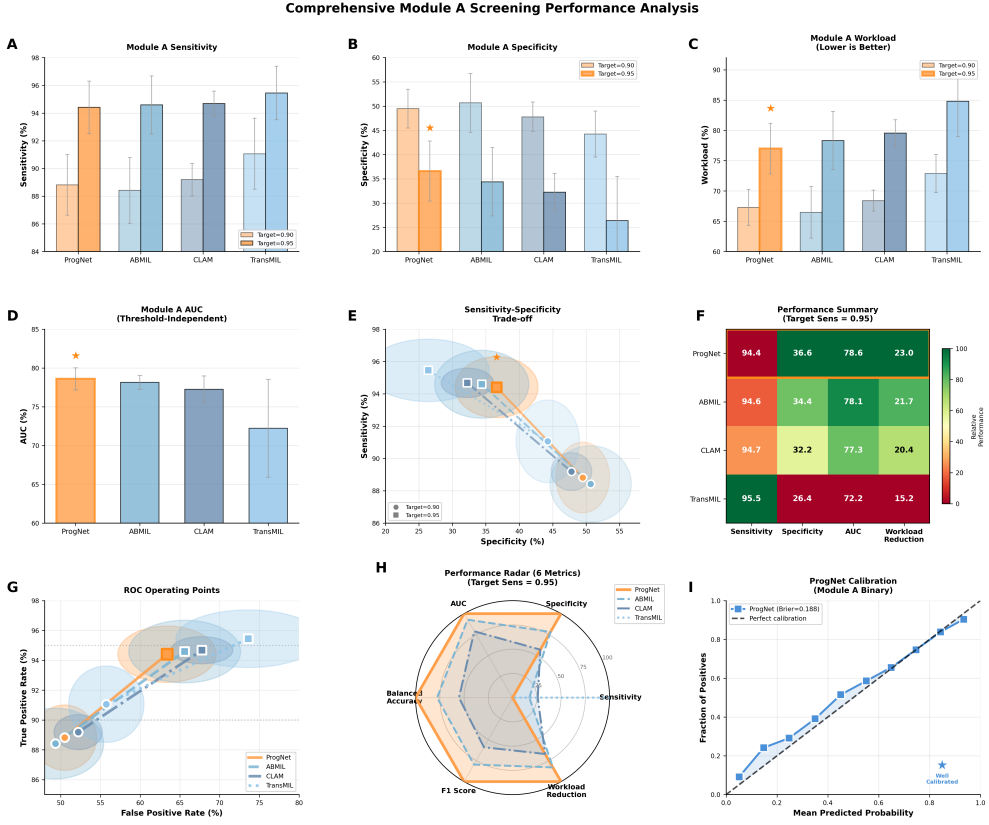


**Fig. 4: Comprehensive evaluation of Module A binary screening performance.**

in Fig. 4 demonstrates that HistoMet produces well-calibrated probability estimates for metastatic risk prediction, supporting the reliability of fixed sensitivity thresholds used in screening-based evaluation. Together, these results indicate that HistoMet can serve as an effective prognostic screening gate by stably separating low-risk primary cases from cases likely to develop metastatic disease.

## 2.5 Effectiveness of Module B for Metastatic Site Prediction

Module B is defined as a conditional predictor of a potential metastatic site given the metastatic potential of Module A. Therefore, to evaluate Module B to demonstrate an upper bound performance independent of upstream screening errors, we first evaluate HistoMet performance on all metastatic cases with available site annotations. This evaluation represents an upper bound with oracle-gated error independent of the errors of Module A.

Under this oracle-gated evaluation, Module B directly models site-specific metastasis patterns among metastatic cases. Given the imbalanced distribution of metastatic sites, we report macro-averaged AUC and Macro-F1 of one-vs. rest as main metrics,

**Performance Comparison Summary**

Method	Top-1 Accuracy (%)	OVR-ROC Macro (%)	Macro F1 (%)
Mean Pooling	74.4 $\pm$ 1.9	85.8 $\pm$ 1.6	69.2 $\pm$ 1.8
Max Pooling	73.2 $\pm$ 2.2	84.4 $\pm$ 1.8	68.7 $\pm$ 1.9
ABMIL 10x	81.8 $\pm$ 1.7	90.1 $\pm$ 1.0	72.2 $\pm$ 1.7
ABMIL 20x	80.9 $\pm$ 1.3	89.9 $\pm$ 1.3	71.8 $\pm$ 1.9
CLAM-SB 10x	76.9 $\pm$ 2.0	87.5 $\pm$ 1.5	71.2 $\pm$ 1.8
CLAM-SB 20x	75.2 $\pm$ 1.7	86.6 $\pm$ 1.3	70.6 $\pm$ 1.5
CLAM-MB 10x	77.8 $\pm$ 2.2	88.0 $\pm$ 2.3	70.9 $\pm$ 2.0
CLAM-MB 20x	76.4 $\pm$ 1.8	86.9 $\pm$ 1.9	70.0 $\pm$ 1.7
TransMIL 10x	79.0 $\pm$ 1.6	88.5 $\pm$ 1.0	70.9 $\pm$ 1.4
TransMIL 20x	78.3 $\pm$ 1.4	87.6 $\pm$ 0.9	70.5 $\pm$ 1.2
VilaMIL	82.5 $\pm$ 1.5	90.8 $\pm$ 1.1	73.2 $\pm$ 1.6
<b>ProgNet (Ours)</b>	<b>84.2 <math>\pm</math> 1.2</b>	<b>92.1 <math>\pm</math> 0.9</b>	<b>74.6 <math>\pm</math> 1.3</b>

**Fig. 5: Comprehensive evaluation of Module B site prediction performance.**

and site-level accuracy as primary metrics. As summarized in Fig. 5, we demonstrate that for metastatic cases, our model achieves the best performance in AUC, ACC, and Macro-F1 and illustrate that it effectively captures discriminative morphological cues associated with different metastatic sites, providing a performance upper bound for decision-aware two-Module Analysis.

Following prior clinical deployment simulations<sup>28–30</sup>, we further validate the end-to-end performance of the two-stage network with different sensitivity-controlled operating point. In this setting, we manually set sensitivity to 95%, 90%, 80%, and 70% on the validation set to determine a decision threshold for Module A metastatic progression prediction (binary), and the selected threshold are subsequently applied to the test cohort without further tuning. These high-sensitivity operating point reflects realistic clinical trade-offs: prioritizing sensitivity reduces the number of missed metastatic cases but increases the number of non-metastatic cases, which are false positives in this scenario. From a clinical perspective, reducing the number of patients incorrectly flagged as high risk is crucial, since each false positive cases incur substantial additional imaging, biopsies, and follow-up visits.

At each sensitivity, Module B assesses only cases predicted to be metastatic from Module A, and produces conditional predictions of metastasis sites, including lymph nodes, liver, brain, and soft tissue. We report Module A sensitivity and specificity on the full test cohort. For decision-aware evaluation, conditional site performance is computed on metastatic cases while explicitly accounting for three clinically relevant outcomes: (1) metastatic cases correctly identified by Module A with accurate site prediction by Module B; (2) metastatic cases missed by Module A that leads to no Module B prediction; and (3) non-metastatic cases incorrectly flagged to Module B, which are contribute to clinical workload but are not included in site prediction accuracy.

Accordingly, we use complementary metrics that account for the aforementioned scenarios in decision-aware modeling. Our metrics include Module A sensitivity and

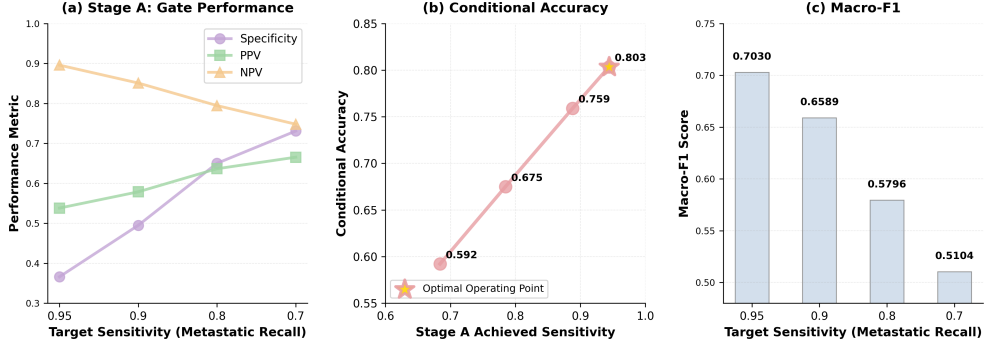


**Fig. 6: Comprehensive evaluation of Module B site prediction performance.**

specificity at each clinical operating points, the fraction of cases blocked by Module A gating, and the conditional two-stage site accuracy among metastatic cases. For two-stage evaluation, we define conditional two-stage site accuracy as the fraction of metastatic cases for which the metastatic site is correctly predicted, where metastatic cases blocked by Module A are counted as incorrect predictions. Fig. 6 summarizes the performance of the proposed decision pipeline across clinically relevant sensitivity-controlled operating points. Under these constraints, HistoMet maintains stable conditional site performance, illustrating robustness of Module B given high-sensitivity screening by metastasis prediction (Module A). These results highlights the practical utility of decoupling metastatic risk prediction (Module A) from downstream conditional metastatic site prediction (Module B) within a clinically motivated two-stage decision pipeline.

## 2.6 Effectiveness of Visual Prototype Token Condensation

Visual prototype condensation is a core component of our proposed HistoMet. The essential goal of this module is to reduce patch-level redundancy and cluster discriminative and relevant morphological visual patterns together. We observe that visual pattern condensation is efficient at grouping similar morphological cues. We validate the effectiveness of this module By comparing Module B variants with a control group without visual prototype condensation, and by performing an ablation study to verify the impact of the number of prototypes on model performance. The ablation study for this module is visualized in Fig. 7a and Fig. 7b.

From the results, we observe that introducing visual prototype token condensation consistently improves model performance across settings, demonstrating that compacting patch-level features into a set of prototype tokens yields more robust site-level feature representations. This improvement demonstrates that Module B benefits from reducing noise by heterogeneous patch-level features and focusing on more discriminative features related to site tropism. From the results, we observe a trade-off between over-compression and representation capacity. As we elaborate on the number of prototype tokens for this module, we observe that when the number of prototype tokens is overly sufficient (over-compression), noise features may persist, leading to condensed

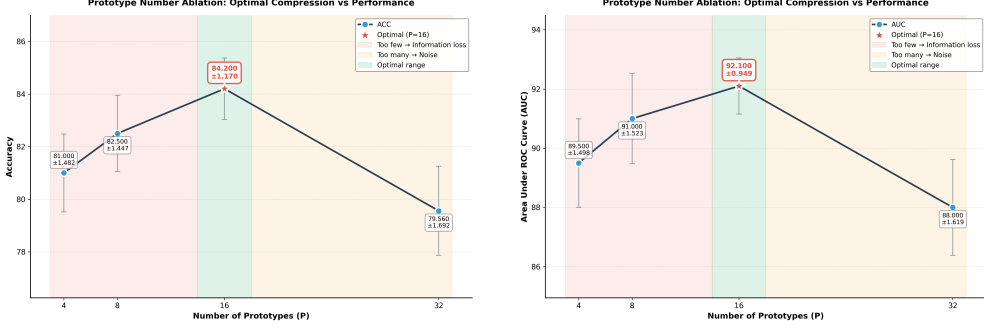


**Fig. 7: Prototype Number Ablation**

representations that include redundant features. On the contrary, when the number of prototype tokens is too few (i.e., aggressive condensation), the loss of fine-grained morphological information would cause a degradation in model performance. Balanced and moderate condensation achieves the best evaluation performance, and we use 16 prototype tokens in our study. Additionally, our results demonstrate performance gains on rare and challenging metastatic sites in our dataset, which typically exhibit greater morphological heterogeneity. We use a variance regularization loss that is applied to each prototype token to reduce intra-prototype variability and explicitly support more consistent representation of each prototype. By utilizing these noise-reduced visual prototype tokens, HistoMet could better align with downstream semantic concept modules to generate more refined features.

## 2.7 Effectiveness of Prototype-level Concept Alignment

Prototype-level concept alignment is an essential component of HistoMet, and these concepts are designed to add interpretability to the visual prototype tokens. HistoMet aligns semantic concepts at the prototype level rather than the concept level, which is efficient because visual prototype condensation already provides regularized, stable feature representations. In this study, we perform an ablation study on using the prototype-level concept alignment. As shown in Fig. 8, introducing prototype-level prompts consistently enhances metastatic site prediction performance across evaluation metrics. The results demonstrate that introducing cancer type-agnostic and site tropism-related prompts at prototype level indeed improve discriminative capability of HistoMet. This enhancement validates that introducing site-relevant morphological cues at prototype-level will help the model to concentrate on crucial regions on the slides, which will enable the model to learn concept aggregated representation that will be crucial for downstream site prediction. Additionally, it is challenging to infer site tropism based on morphological cues, so our prototype level prompts are generated based on answers generated by frozen LLM that potentially indicate site tropism. We define prompt at 10x magnifications to capture more global architectural and tissue-level morphological patterns such as growth siteization, and we define prompt at 20×

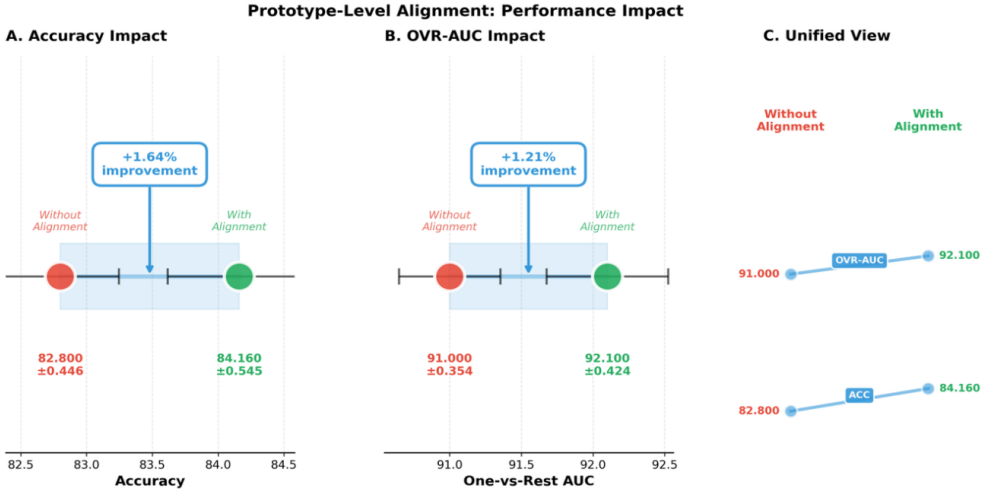


**Fig. 8: Model performance with and without prototype-level concept alignment**

magnification to focus on fine-grained morphology. Our proposed multi-scale prototype level concept alignment integrates complementary and useful semantics to each visual patterns. Therefore, we could interpret the downstream performance gain by feature representations at prototype level.

## 2.8 Effectiveness of Class-level (Site-level) Semantic Prompts

We further validate the effectiveness of class-level prompt for Module B. Before site-level prediction, our model will utilize high-level class-level concepts that encode site-specific priors, so the model will be able to weight concept-aggregated slide representations from the prototype level into the final slide-level feature representations.

As shown in Fig. 9, removing class-level concept alignment leads to consistent degradation in metastatic site prediction performance. When we exclude site-level concept alignment, the AUC dropped by 0.77%, which indicates that simple slide-level aggregation is insufficient to make satisfying site predictions. The experimental results demonstrate the significance of bag-level concept alignment that encodes global contextual information. By integrating site-specific concepts during bag-level representations, HistoMet explicitly learns to efficiently aggregate morphological patterns to metastatic site, indicating its capability in prognostics. The bag-level concept alignment introduces interpretability as concept-level alignment, enhancing the discriminative performance overall. Overall, the effectiveness of class-level concept alignment provides high-level complementary information that enables more realistic metastatic site prediction.

Multi-scale fusion is an essential design in HistoMet, motivated by the need to capture complementary morphological patterns observable at multiple resolutions for downstream metastatic site classification. Specifically, we use 10x and 20x magnification in our framework, and 10x magnification captures global architecture and

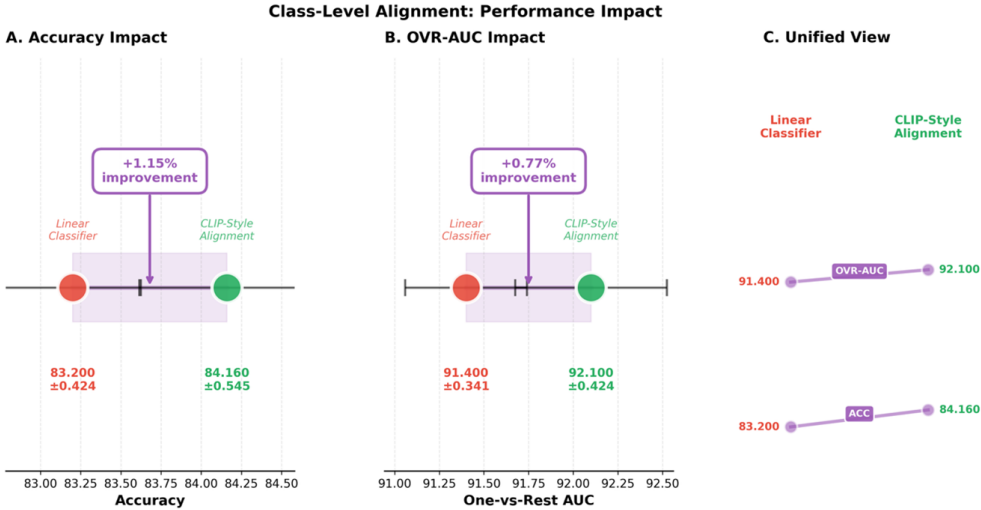


Fig. 9: Model performance with and without class-level concept alignment

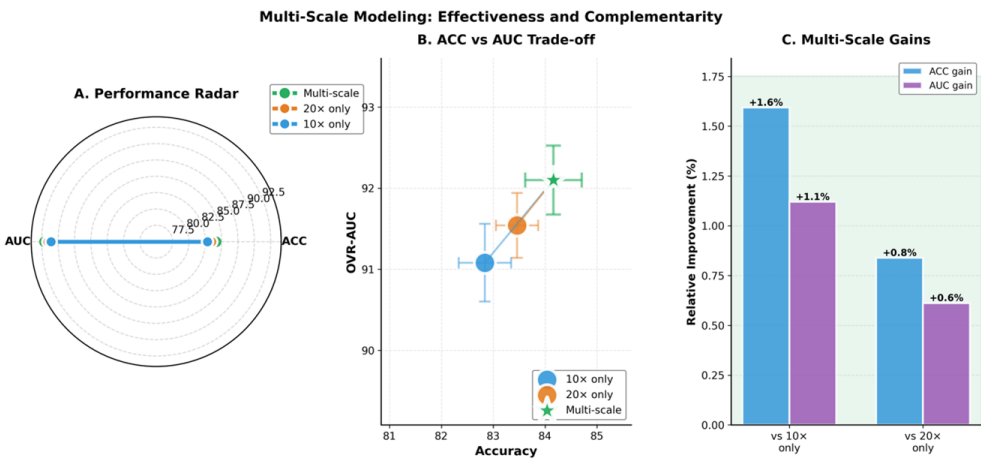
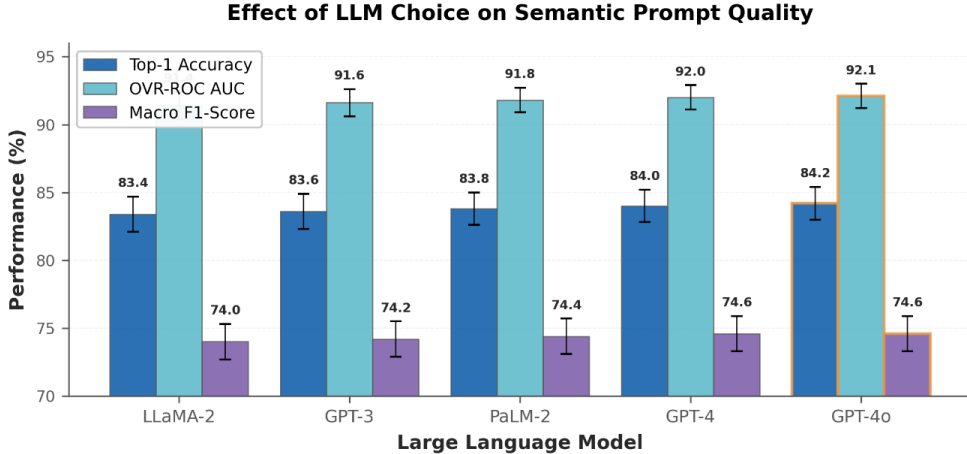


Fig. 10: Model performance with and without multi-scale fusion

growth siteizations, while 20x magnification provides more fine-grained cellular and microstructural features that might be indicative of site tropism prediction. We perform a validation study on HistoMet and compare baselines with single magnifications; we demonstrate that, with multiple magnifications, HistoMet outperforms all comparison methods. As shown in Fig. 10, integrating multi-scale logit-level fusion consistently improves metastatic site prediction performance across all evaluation metrics. When operating at low magnification, HistoMet efficiently leverages global context, but fine-grained cellular information is lacking; at high magnification, HistoMet leverages fine-grained cellular context but lacks sufficient architectural patterns. Multi-scale



**Fig. 11: Model performance with different LLMs**

logit-level fusion combines prediction logits after a slide-level prediction, efficiently integrating complementary scale predictions across resolutions. Notably, multi-scale modelling enhances model performance through logit-level fusion, suggesting that combining scale-specific predictions provides useful and complementary information. Logit-level fusion reduces bias and error while combining global and cellular information in a robust manner. Therefore, this study illustrates that multi-scale modeling is an essential component of HistoMet, enhancing the robustness and site-reliable prediction.

## 2.9 Comparison of different large language models

To validate the semantic prompt quality on HistoMet, we compare evaluation performance across different LLMs that generate prompts at the prototype and class levels. In our study, the overall training protocols were fixed, and we varied the LLMs we used for the experiments. As shown in Fig. 11, more advanced LLMs achieve better performance on the site prediction task. In particular, prompts generated by GPT-5 yield the strongest performance. We believe that higher-quality prompts will be more semantically rich, enhancing downstream concept alignment at the prototype and class levels. The experimental results demonstrate that HistoMet efficiently leverages semantic prompts and uses them as a guide for aggregation.

## 2.10 Model Interpretation and Qualitative Analysis

Model interpretability is critical for clinical deployment of computational pathology systems. In Fig. , we provide visualization results for interpretability at prototype level and to validate semantically meaningful regions that would contribute to site prediction. Specifically, HistoMet generates prototype-level similarity map to indicate regions particularly associated with a given morphological concepts that might be indicative of metastatic potential. Representative qualitative examples are shown in Fig. 10

where we visualize prototype-level concepts based on primary tumor morphology that are indicative of potential metastasis. These attention maps demonstrate that HistoMet specifically focuses on clinically meaningful tumor regions that could be meaningful for metastatic studies, such as invasive tumor fronts and tumor budding, which are morphological visual patterns we define to be meaningful to metastasis. Compared with comparison methods like ABMIL and CLAM, HistoMet provides more consistent and coherent visual patterns as we have refined prototype tokens for alignment. After reviewing of our collaborating pathologist, we confirmed that regions underscored by HistoMet align with morphologically meaningful tissue patterns relevant to predict metastatic potential. These visual patterns are commonly recognized in real-world clinical settings and provide visual anchor for pathologist to analyze metastatic potential based on primary tumor histology. Besides highlighting individual regions, HistoMet demonstrates that multiple prototype level concepts contribute simultaneously to a single metastatic site prediction. This is different from attention mechanisms<sup>31</sup> that only highlights a few patches from the WSIs, HistoMet integrates evidence from diverse prototype activation, taking advantage of heterogenous morphological cues that are useful for downstream classification.

## 2.11 Discussion

Despite substantial progress in computational pathology (CPath), predicting metastatic potential and the metastatic site based on primary tumor morphology remains a fundamental challenge. Most existing studies focus on diagnostic tasks, such as detecting metastatic deposits within an site, which are basically retrospective classifications based on metastatic tissue slides. In contrast, predicting metastatic potential as a prognostic task remains challenging and largely unexplored in existing research. This prognostic modelling is of great clinical significance, such as enabling early intervention and treatment planning. Recent advances in pathology vision–language foundation models have paved the way to bridge histopathological imaging with human-interpretable semantic knowledge. By aligning visual representations with pathology meaningful concepts, these models offer a promising pathway toward interpretable and decision-aware WSI analysis. However, randomly applying language models or text prompts to pathology images might introduce hallucinated associations that are not biologically meaningful. Additionally, the challenging nature of prognostic modelling of metastatic progression might exceed the scope of human-defined priors, therefore promoting the need to discover data-adaptive and complementary morphological patterns associated with large-scale pathology datasets.

To address these challenges, we propose HistoMet, a prognostic framework that integrates linguistically defined morphological concepts with data-adaptive visual representations to predict metastatic progression from primary tumor WSIs. Unlike conventional diagnostic frameworks, HistoMet explicitly formulates metastatic outcome prediction as a two-stage, decision-aware pipeline. Module A’s function is to prioritize a high-sensitivity gate at a particular operating point, while Module B conditionally models metastatic site tropism among predicted high-risk tasks. This decoupled design is similar to the real-world clinical decision-making process and makes HistoMet highly deployable in clinical settings.

HistoMet leverages a cross-attention mechanism to condense visually heterogeneous patches into compact, robust visual prototype tokens and aligns these prototypes using a pathology-focused vision-language model. This vision language alignment enables HistoMet to leverage the semantic structure of large-scale pretrained models without relying on explicitly curated expert priors. Essentially, HistoMet operates on primary tumor histology and integrates multi-scale, prediction-level fusion to provide robust, reliable slide-level predictions. For visual prototypes and concept tokens, they are both learnable and data-adaptive, maintaining the generalization ability of the pathology foundational vision-language model while self-adapting to dataset attributes. Across extensive qualitative and quantitative evaluations, HistoMet outperforms existing baselines for predicting metastatic potential and metastatic site prediction.

Despite these encouraging results, HistoMet has some limitations that needs to be discussed. First, while HistoMet integrates LLM-defined concepts to enhance interpretability, the completeness and accuracy of these concepts remain limited, particularly for rare, under-characterized metastasis. Because LLMs might hallucinate, concepts require human experts to proofread before feeding them into the model. Additionally, although visual prototype condensation provides more robust, compact visual feature representations, fully interpreting these representations requires expert pathologists. Thirdly, the vision-language encoders are kept frozen and not explicitly adapted to the downstream prognostic task. Although learnable prompts enable task-specific semantic guidance at the prototype level, the parameters of the frozen text encoder are kept frozen and not fine-tuned for the downstream prognostic task. Future work will expand HistoMet in several possible directions. We plan to explore adaptive finetuning of vision-language encoders, such as using adapters, to better align feature representations for downstream usage. Besides, we plan to integrate ensemble learning to improve robustness and reliability, such as aggregation across multiple scales. Ensemble learning might further reduce variance and enhance model performance, particularly for rare metastatic site prediction.

### 3 Methods

#### 3.1 Overview of HistoMet

Fig. 1 presents an overview of the proposed HistoMet framework for metastatic site tropism prediction from primary tumor histology. HistoMet applies a two-stage decision-aware pipeline that explicitly decouples metastatic potential from metastatic site prediction. In Module A, the HistoMet operates at high-sensitivity-based operating points and generates probabilities of primary vs. metastatic disease to reduce false positives. Module A’s design is to minimize false positives and pass cases predicted to metastasize to Module B for downstream analysis.

Module B’s design aims to predict metastatic site tropism by aligning compact, coherent visual patterns with semantic guidance. Specifically, patch-level features extracted from pathology foundational models are condensed into a set of learnable visual prototypes. This prototype summarizes relevant morphological cues while reducing the noisy patch features using our proposed regularizing loss. To improve

interpretability and visual-semantic alignment, HistoMet uses metastasis-relevant semantic prompts to align with these condensed visual prototypes. After prototype-level alignment, these concept-aggregated feature representations will be further aligned with class-level concepts, and these semantic concepts will guide the HistoMet to generate reliable and robust slide-level predictions.

To capture complementary information across magnifications, HistoMet processes WSIs at 10x and 20x magnifications. Each magnification independently produces site-level prediction logits, which are fused at the subsequent site level to generate the final slide-level prediction. This design performs logit-level multi-scale fusion via majority voting to provide complementary information across scales. After retrieving bag-level representations, HistoMet integrates class-level concept embeddings to compute similarity scores and generate the final site prediction. For clarity, the formulations in the following sections focus on the Module B multi-class metastatic site prediction task.

### 3.2 Visual Prototype Condensation

Whole-slide images contain a large number of instance-level patch features, many of which are redundant or weakly informative for metastatic site prediction. Aggregating all patch features not only computationally inefficient but also introduce redundant signals during slide level aggregation. To address this challenge, HistoMet decomposes the patch-level feature representation of a WSI into a condensed set of visual prototype tokens through cross attention mechanism.

Specifically, visual prototype condensation first initializes learnable prototype vectors, and then aggregates patch-level features into each learnable prototype representation, each summarizing a recurrent morphological pattern across patches. These prototype tokens are optimized end-to-end using the training data and are adaptively learned to aggregate visual patterns. As a result, prototype condensation captures complementary visual evidence beyond individual patch features and substantially reduces redundant feature representations.

Additionally, visual prototype condensation differs from semantic prompting in both its generation mechanism and objective. Prototype tokens are purely learnable, data-driven and optimized by end-to-end gradient optimization. Prototype condensation aims to provide stable, compact, and noise-robust visual representations that function as an effective interface for later bag-level aggregation and semantic alignment instead of introducing new semantic anchors. By condensing patch-level information into coherent and robust prototype-level representations, HistoMet simplifies downstream modeling and improves robustness in metastatic site prediction.

#### *Cross-attention based prototype condensation.*

Given a WSI  $X$ , we tile it into  $N$  patches and extract patch embeddings using a frozen feature encoder. At a fixed magnification, let

$$\mathbf{M} = [\mathbf{m}_1, \dots, \mathbf{m}_N]^\top \in \mathbb{R}^{N \times L} \quad (1)$$

denote the instance-level patch features with embedding dimension  $L$ . We introduce  $P$  learnable prototype centers (query tokens),

$$\mathbf{C} = [\mathbf{c}_1, \dots, \mathbf{c}_P]^\top \in \mathbb{R}^{P \times L}, \quad (2)$$

Prototype condensation is implemented via a single-head cross-attention operator  $\text{Attn}(\cdot)$  that maps  $(\mathbf{C}, \mathbf{M})$  to condensed prototype tokens:

$$\mathbf{H} = \text{Attn}(\mathbf{C}, \mathbf{M}, \mathbf{M}) \in \mathbb{R}^{P \times L}. \quad (3)$$

Concretely, with linear projections  $\mathbf{W}_Q, \mathbf{W}_K, \mathbf{W}_V \in \mathbb{R}^{L \times L}$ ,

$$\mathbf{Q} = \mathbf{C}\mathbf{W}_Q \in \mathbb{R}^{P \times L}, \quad (4)$$

$$\mathbf{K} = \mathbf{M}\mathbf{W}_K \in \mathbb{R}^{N \times L}, \quad (5)$$

$$\mathbf{V} = \mathbf{M}\mathbf{W}_V \in \mathbb{R}^{N \times L}, \quad (6)$$

and attention weights (prototype-to-instance) are

$$\mathbf{A} = \text{softmax}\left(\frac{\mathbf{Q}\mathbf{K}^\top}{\sqrt{L}}\right) \in \mathbb{R}^{P \times N}, \quad \sum_{i=1}^N A_{pi} = 1. \quad (7)$$

The condensed prototypes are then

$$\mathbf{H} = \mathbf{AV} \in \mathbb{R}^{P \times L}. \quad (8)$$

We apply a residual update followed by layer normalization to stabilize optimization:

$$\mathbf{H} \leftarrow \text{LN}(\mathbf{H} + \mathbf{C}). \quad (9)$$

#### ***Prototype compactness via attention-weighted variance.***

To encourage each prototype to maintain coherent feature representations that better align with semantic concept alignment, we use the attention weights to regularize the dispersion of instances assigned to each prototype. Optionally, we  $\ell_2$ -normalize features before measuring dispersion (enabled in our implementation):

$$\bar{\mathbf{m}}_i = \frac{\mathbf{m}_i}{\|\mathbf{m}_i\|_2}, \quad \bar{\mathbf{h}}_p = \frac{\mathbf{h}_p}{\|\mathbf{h}_p\|_2}. \quad (10)$$

We define the attention-weighted per-prototype variance as

$$v_p = \sum_{i=1}^N A_{pi} \|\bar{\mathbf{m}}_i - \bar{\mathbf{h}}_p\|_2^2, \quad p = 1, \dots, P, \quad (11)$$

and the compactness regularizer

$$\mathcal{L}_{\text{compact}} = \frac{1}{P} \sum_{p=1}^P v_p. \quad (12)$$

For multi-scale inputs, we compute  $\mathcal{L}_{\text{compact}}$  independently at each magnification (e.g.,  $10\times$  and  $20\times$ ) and sum them:

$$\mathcal{L}_{\text{compact}}^{\text{total}} = \mathcal{L}_{\text{compact}}^{(10\times)} + \mathcal{L}_{\text{compact}}^{(20\times)}. \quad (13)$$

The overall training objective integrates the task loss  $\mathcal{L}_{\text{task}}$  with the compactness loss term:

$$\mathcal{L} = \mathcal{L}_{\text{task}} + \lambda_{\text{compact}} \mathcal{L}_{\text{compact}}^{\text{total}}, \quad (14)$$

where  $\lambda_{\text{compact}}$  specifies the strength of the prototype regularizer. The module outputs the condensed visual prototype token  $\mathbf{H} \in \mathbb{R}^{P \times L}$  (per magnification), which serves as the input to subsequent prototype-level concept alignment.

### 3.3 Semantic alignment between condensed visual prototype with learnable semantic concept

To integrate interpretability to HistoMet, we use semantic site tropism-related concepts to align visual prototype tokens in feature space. In HistoMet, this alignment is performed using a set of learnable data-driven instance-level concepts following the style in [29]. This Coop-style learnable concepts are data-adaptive and will be optimized based on dataset attributes on the text side by the training objective.

Given a condensed prototype representation  $\mathbf{H} = \{\mathbf{h}_1, \dots, \mathbf{h}_P\}$ ,  $\mathbf{h}_p \in \mathbb{R}^L$ , we introduce a set of  $M$  learnable concept embeddings  $\mathbf{C} = \{\mathbf{c}_1, \dots, \mathbf{c}_M\}$ ,  $\mathbf{c}_m \in \mathbb{R}^L$ . These prompts are generated by querying frozen LLMs to produce site tropism morphological features; these concepts are purely data-adaptive and do not correspond to predefined morphological labels. They are optimized to capture latent visual patterns that are predictive of metastatic site outcomes.

To align prototype tokens with the learned concepts, we compute a prototype-concept similarity matrix using cosine similarity:

$$s_{p,m} = \cos(\mathbf{h}_p, \mathbf{c}_m), \quad p = 1, \dots, P, \quad m = 1, \dots, M. \quad (15)$$

For each concept  $m$ , similarities across prototypes are normalized using a softmax operation:

$$\alpha_{p,m} = \frac{\exp(s_{p,m})}{\sum_{p'=1}^P \exp(s_{p',m})}, \quad (16)$$

yielding a set of attention weights that indicate the relevance of each prototype token to the given concept.

Using these weights, concept-aligned visual representations are obtained by aggregating prototype tokens:

$$\mathbf{v}_m = \sum_{p=1}^P \alpha_{p,m} \mathbf{h}_p, \quad (17)$$

where  $\mathbf{v}_m \in \mathbb{R}^L$  summarizes the visual evidence associated with concept  $m$  across the entire slide. Essentially, the learned visual prototype tokens are aggregated to the concept-level feature space. Therefore, complex, heterogeneous features are projected into a structured, concept-specific feature space.

Finally, the slide-level representation is obtained by aggregating across all learned concepts:

$$\mathbf{z} = \frac{1}{M} \sum_{m=1}^M \mathbf{v}_m. \quad (18)$$

This concept-guided aggregation operates entirely at the prototype level, avoiding direct dependence on instance-level patch features. As a result, semantic alignment is performed on compact, regularized representations rather than noisy local features.

### 3.4 Hierarchical Two-stage Concept-guided Aggregation

HistoMet performs bag-level aggregation in a hierarchical, concept-guided manner. Conventional multiple instance learning typically pool or use attention to aggregate instance level features, HistoMet first condenses patch-level representations into a compact set of visual prototype tokens (Sec. ??), and subsequently aggregates these prototype tokens into concept-aligned representations prior to slide-level classification. This two-Module Aggregation strategy explicitly decomposes the bag representation learning process into (i) prototype-to-concept alignment and (ii) concept-to-bag alignment and prediction, mimicing how pathologists sequentially make inferences from local fine grained context to global summarization.

For a given magnification  $s \in \{\text{low, high}\}$ , let  $\mathbf{H}^{(s)} \in \mathbb{R}^{P \times L}$  denote the set of condensed visual prototype tokens, where each row  $\mathbf{h}_p^{(s)} \in \mathbb{R}^L$  summarizes a recurrent morphological pattern across the slide. We further introduce a set of learnable concept prompt embeddings  $\mathbf{U}^{(s)} \in \mathbb{R}^{M \times L}$ , with rows  $\mathbf{u}_m^{(s)} \in \mathbb{R}^L$ , as well as class-level (metastatic site) prompt embeddings  $\mathbf{T}^{(s)} \in \mathbb{R}^{C \times L}$ , with rows  $\mathbf{t}_c^{(s)} \in \mathbb{R}^L$ . All embeddings are  $\ell_2$  normalized prior to similarity computation.

In the first aggregation stage, HistoMet aligns visual prototype tokens with semantic concepts by computing a prototype-concept similarity matrix via cosine similarity:

$$\mathbf{S}^{(s)} = \mathbf{H}^{(s)} (\mathbf{U}^{(s)})^\top \in \mathbb{R}^{P \times M}, \quad S_{p,m}^{(s)} = \cos(\mathbf{h}_p^{(s)}, \mathbf{u}_m^{(s)}). \quad (19)$$

For each concept  $m$ , similarities are normalized across prototypes to obtain concept-conditioned attention weights:

$$\alpha_{p,m}^{(s)} = \frac{\exp(S_{p,m}^{(s)})}{\sum_{p'=1}^P \exp(S_{p',m}^{(s)})}. \quad (20)$$

These weights indicate the relevance of each prototype token to a given semantic concept. Concept-aligned visual representations are then computed as weighted combinations of prototype tokens:

$$\mathbf{v}_m^{(s)} = \sum_{p=1}^P \alpha_{p,m}^{(s)} \mathbf{h}_p^{(s)}, \quad \mathbf{V}^{(s)} = \{\mathbf{v}_m^{(s)}\}_{m=1}^M \in \mathbb{R}^{M \times L}. \quad (21)$$

Each  $\mathbf{v}_m^{(s)}$  thus aggregates slide-level evidence aligned with concept  $m$  by selectively attending to relevant prototype tokens.

In the second aggregation stage, the concept-aligned representations are summarized into a scale-specific slide embedding. In the default setting, HistoMet applies simple mean pooling across concepts:

$$\mathbf{z}^{(s)} = \frac{1}{M} \sum_{m=1}^M \mathbf{v}_m^{(s)} \in \mathbb{R}^L. \quad (22)$$

To produce metastatic site predictions, the resulting slide embedding  $\mathbf{z}^{(s)}$  is aligned with class-level prompts in a CLIP-style manner:

$$\ell^{(s)} = \lambda \mathbf{z}^{(s)} (\mathbf{T}^{(s)})^\top \in \mathbb{R}^C, \quad \ell_c^{(s)} = \lambda \cos(\mathbf{z}^{(s)}, \mathbf{t}_c^{(s)}), \quad (23)$$

where  $\lambda$  is a fixed temperature parameter controlling logit sharpness. Class probabilities are obtained via  $\mathbf{p}^{(s)} = \text{Softmax}(\ell^{(s)})$ .

After generating the slide-level feature representation during the forward pass, HistoMet computes logits independently for each scale and fuses them at the decision level:

$$\ell = \ell^{(\text{low})} + \ell^{(\text{high})}, \quad (24)$$

The final prediction for each class is given by  $\mathbf{p} = \text{Softmax}(\ell)$ .

Overall, this hierarchical aggregation at the prototype and class levels differs significantly from standard MIL. This design yields compact and stable slide embeddings that improve robustness while enabling concept-aware interpretation of metastatic site predictions.

---

**Algorithm 1:** MyModelEntity: Multi-scale Prototype MIL with Instance Prompting

---

**Input:** Low-scale patch features  $X^{(s)} \in \mathbb{R}^{N_s \times L}$ ; (optional) high-scale patch features  $X^{(l)} \in \mathbb{R}^{N_l \times L}$ ; number of classes  $C$ ; number of prototypes  $P$ ; instance prompts  $\mathcal{P}_{\text{inst}}$  and class prompts  $\mathcal{P}_{\text{cls}}^{(s)}, \mathcal{P}_{\text{cls}}^{(l)}$ .

**Output:** Class logits  $\ell \in \mathbb{R}^C$  and probabilities  $p \in \mathbb{R}^C$ .

```

1 Precompute text embeddings (frozen text encoder);
2  $T_{\text{inst}}^{(s)} \leftarrow \text{Normalize}(f_{\text{text}}(\mathcal{P}_{\text{inst}}^{(s)}))$ ;
3  $T_{\text{inst}}^{(l)} \leftarrow \text{Normalize}(f_{\text{text}}(\mathcal{P}_{\text{inst}}^{(l)}))$ ;
4  $T_{\text{cls}}^{(s)} \leftarrow \text{Normalize}(f_{\text{text}}(\mathcal{P}_{\text{cls}}^{(s)})) \in \mathbb{R}^{C \times L}$ ;
5  $T_{\text{cls}}^{(l)} \leftarrow \text{Normalize}(f_{\text{text}}(\mathcal{P}_{\text{cls}}^{(l)})) \in \mathbb{R}^{C \times L}$ ;
6 Prototype compression (shared across scales);
7 Initialize learnable prototype queries  $Q \in \mathbb{R}^{P \times L}$ ;
8 for  $scale r \in \{s, l\}$  do
9   if  $X^{(r)}$  is provided then
10    |  $(H^{(r)}, A^{(r)}) \leftarrow \text{CrossAttn}(Q, X^{(r)})$  ;  $// H^{(r)} \in \mathbb{R}^{P \times L}$ 
11    |  $H^{(r)} \leftarrow \text{LayerNorm}(H^{(r)} + Q)$ ;
12   else
13    | continue;
14 Instance prompting (token  $\rightarrow$  concept aggregation);
15 for  $r \in \{s, l\}$  do
16   if  $H^{(r)}$  exists then
17    |  $\hat{H}^{(r)} \leftarrow \text{Normalize}(H^{(r)})$ ;
18    |  $\hat{T}_{\text{inst}}^{(r)} \leftarrow \text{Normalize}(T_{\text{inst}}^{(r)})$ ;
19    |  $S^{(r)} \leftarrow \hat{H}^{(r)} \left( \hat{T}_{\text{inst}}^{(r)} \right)^{\top} \in \mathbb{R}^{P \times M}$ ;
20    |  $W^{(r)} \leftarrow \text{Softmax}_P(S^{(r)})$  ;  $// \text{normalize over prototypes for each concept}$ 
21    |  $V^{(r)} \leftarrow (W^{(r)})^{\top} H^{(r)} \in \mathbb{R}^{M \times L}$  ;  $// \text{concept-specific visual tokens}$ 
22    |  $z^{(r)} \leftarrow \frac{1}{M} \sum_{m=1}^M V_m^{(r)} \in \mathbb{R}^L$  ;  $// \text{scale embedding}$ 
23 Class alignment (CLIP-style);
24 for  $r \in \{s, l\}$  do
25   if  $z^{(r)}$  exists then
26    |  $\hat{z}^{(r)} \leftarrow \text{Normalize}(z^{(r)})$ ;
27    |  $\ell^{(r)} \leftarrow \tau \cdot \hat{z}^{(r)} \left( T_{\text{cls}}^{(r)} \right)^{\top} \in \mathbb{R}^C$ ;
28 Multi-scale fusion;
29 if  $\ell^{(s)}$  and  $\ell^{(l)}$  both exist then
30  |  $\ell \leftarrow \ell^{(s)} + \ell^{(l)}$  ;  $// \text{sum fusion}$ 
31 else
32  |  $\ell \leftarrow \ell^{(s)}$  ;  $// \text{single-scale fallback}$ 
33  $p \leftarrow \text{Softmax}(\ell)$ ;
34 return  $\ell, p$ ;

```

---

## 4 Data preprocessing

In our study, whole slide images (WSIs) were preprocessed to extract patch-level representations at multiple spatial resolutions. Tissue regions were first automatically segmented using Otsu thresholding in the HSV color space to exclude non-tissue background. The segmented tissue regions were then cropped into non-overlapping  $256 \times 256$  pixel patches at two magnification levels:  $10\times$  and  $20\times$ . In our study, we use the pathology foundational model Conch to generate the patch level feature representations. Conch encodes each patch into a 512-dimensional feature vector and has been pre-trained on over one million histopathology image–caption pairs. For each WSI, extracted features and their corresponding spatial coordinates were stored in HDF5 format for downstream multiple instance learning. To guarantee data quality, slides with insufficient tissue content and background-dominated areas were eliminated. This process ensures that the patches are representatives of histology and capture critical information for downstream analysis.

## 5 Baseline models

Multiple Instance Learning (MIL) [9] has become a standard framework for whole-slide image (WSI) analysis under weak supervision. Slide level prediction are generated by aggregation of heterogenous patches. While recent studies [30–32] are mainly focused on enhancing visual feature aggregation mechanism, they primarily relied on imaging modality and does not leverage multimodal information to add interpretability. These interpretability could be achieved by language modality, for our downstream task, language guided priors such as morphological patterns associated with invasion, dissemination, and disease progression could be integrated to interpret visual patterns from a particular slide. Therefore, existing MIL are limited in their ability to represent high-level semantic concepts that are critical for prognostic-related downstream tasks. We compare HistoMet to a comprehensive set of MIL that are commonly adopted in diagnostic and prognostic downstream tasks.

## 6 Training details

All experiments were conducted on NVIDIA A100 GPUs. We used the CONCH vision–language foundation model (ViT-B/16) as a frozen feature extractor for both histopathology image patches and textual concepts. Whole-slide images were processed at  $10\times$  and  $20\times$  magnification, and each  $256 \times 256$  patch was encoded into a 512-dimensional feature vector. HistoMet employs a dual-scale attention-based multiple instance learning architecture with 16 learnable visual prototypes per scale and learnable text concepts. During training, we kept the CONCH visual and text encoder to be frozen. Prototype compactness was encouraged using a variance regularization term ( $\lambda = 0.001$ ). The model was trained using the Adam optimizer with a learning rate of 0.0001 with early stopping. Evaluation was performed using patient-level five-fold cross-validation, reporting mean  $\pm$  standard deviation across folds. For evaluation metrics, the area under the curve (AUC) and accuracy (ACC) were adopted.

## References

- [1] Swanson, K., Wu, E., Zhang, A., Alizadeh, A.A., Zou, J.: From patterns to patients: Advances in clinical machine learning for cancer diagnosis, prognosis, and treatment. *Cell* **186**(8), 1772–1791 (2023)
- [2] Lee, M.: Recent advancements in deep learning using whole slide imaging for cancer prognosis. *Bioengineering* **10**(8), 897 (2023)
- [3] Andrew, T.W., Combalia, M., Hernandez, C., Grant, S., Paragh, G., Puig, S., Mc Arthur, G., Richardson, G., Sloan, P., Shalhout, S.Z., *et al.*: Multimodal ai and tumour microenvironment integration predicts metastasis in cutaneous melanoma. *Nature Communications* **16**(1), 10095 (2025)
- [4] Yang, L., Yang, J., Kleppe, A., Danielsen, H.E., Kerr, D.J.: Personalizing adjuvant therapy for patients with colorectal cancer. *Nature Reviews Clinical Oncology* **21**(1), 67–79 (2024)
- [5] Zang, X., Xia, Y., Xiao, H., Luo, H., Si, M., Hou, N., Haoni, A., Chen, T., Liu, Z., Pu, X., *et al.*: A multimodal ai model for precision prognosis in clear cell renal cell carcinoma: A multicenter study. *npj Digital Medicine* **8**(1), 668 (2025)
- [6] El Nahhas, O.S., Loeffler, C.M., Carrero, Z.I., Treeck, M., Kolbinger, F.R., Hewitt, K.J., Muti, H.S., Graziani, M., Zeng, Q., Calderaro, J., *et al.*: Regression-based deep-learning predicts molecular biomarkers from pathology slides. *Nature communications* **15**(1), 1253 (2024)
- [7] Chen, R.J., Lu, M.Y., Wang, J., *et al.*: Pathomic fusion: An integrated framework for fusing histopathology and genomic features for cancer diagnosis and prognosis. In: *MICCAI* (2021)
- [8] Campanella, G., Hanna, M.G., Geneslaw, L., Miraflor, A., Werneck Krauss Silva, V., Busam, K.J., Brogi, E., Reuter, V.E., Klimstra, D.S., Fuchs, T.J.: Clinical-grade computational pathology using weakly supervised deep learning on whole slide images. *Nature medicine* **25**(8), 1301–1309 (2019)
- [9] Ilse, M., Tomczak, J., Welling, M.: Attention-based deep multiple instance learning. In: *International Conference on Machine Learning*, pp. 2127–2136 (2018). PMLR
- [10] Lu, M.Y., Williamson, D.F.K., Chen, T.Y., *et al.*: Data-efficient and weakly supervised computational pathology on whole-slide images. *Nature Biomedical Engineering* (2021)
- [11] Shao, Z., Bian, H., Chen, Y., *et al.*: Transmil: Transformer based correlated multiple instance learning for whole slide image classification. In: *NeurIPS* (2021)

- [12] Radford, A., Kim, J.W., Hallacy, C., Ramesh, A., Goh, G., Agarwal, S., Sastry, G., Askell, A., Mishkin, P., Clark, J., *et al.*: Learning transferable visual models from natural language supervision. In: International Conference on Machine Learning, pp. 8748–8763 (2021). PmLR
- [13] Gamper, J., Rajpoot, N.: Multiple instance captioning: Learning representations from histopathology textbooks and articles. In: Proceedings of the IEEE/CVF Conference on Computer Vision and Pattern Recognition, pp. 16549–16559 (2021)
- [14] Lu, M.Y., Chen, B., Zhang, A., Williamson, D.F., Chen, R.J., Ding, T., Le, L.P., Chuang, Y.-S., Mahmood, F.: Visual language pretrained multiple instance zero-shot transfer for histopathology images. In: Proceedings of the IEEE/CVF Conference on Computer Vision and Pattern Recognition, pp. 19764–19775 (2023)
- [15] Huang, Z., Bianchi, F., Yuksekgonul, M., Montine, T.J., Zou, J.: A visual–language foundation model for pathology image analysis using medical twitter. *Nature medicine* **29**(9), 2307–2316 (2023)
- [16] Shu, H., Li, J., Wang, S.: Vision-language multiple instance learning for histopathology. In: ICLR (2024)
- [17] Zhou, J., Shao, W., Yue, Y., Mu, W., Wan, P., Zhu, Q., Zhang, D.: Maple: Multi-scale attribute-enhanced prompt learning for few-shot whole slide image classification. arXiv preprint arXiv:2509.25863 (2025)
- [18] Han, M., Qu, L., Yang, D., Zhang, X., Wang, X., Zhang, L.: Mscpt: Few-shot whole slide image classification with multi-scale and context-focused prompt tuning. *IEEE Transactions on Medical Imaging* (2025)
- [19] Qu, L., Fu, K., Wang, M., Song, Z., *et al.*: The rise of ai language pathologists: Exploring two-level prompt learning for few-shot weakly-supervised whole slide image classification. *Advances in Neural Information Processing Systems* **36**, 67551–67564 (2023)
- [20] Ferber, D., Wölflein, G., Wiest, I.C., Ligero, M., Sainath, S., Ghaffari Laleh, N., El Nahhas, O.S., Müller-Franzes, G., Jäger, D., Truhn, D., *et al.*: In-context learning enables multimodal large language models to classify cancer pathology images. *Nature Communications* **15**(1), 10104 (2024)
- [21] Zhang, K., Zhou, R., Adhikarla, E., Yan, Z., Liu, Y., Yu, J., Liu, Z., Chen, X., Davison, B.D., Ren, H., *et al.*: A generalist vision–language foundation model for diverse biomedical tasks. *Nature Medicine* **30**(11), 3129–3141 (2024)
- [22] Vorontsov, E., Bozkurt, A., Casson, A., Shaikovski, G., Zelechowski, M., Severson, K., Zimmermann, E., Hall, J., Tenenholz, N., Fusi, N., *et al.*: A foundation model

for clinical-grade computational pathology and rare cancers detection. *Nature medicine* **30**(10), 2924–2935 (2024)

- [23] Kather, J.N., Heij, L.R., Grabsch, H.I., Loeffler, C., Echle, A., Muti, H.S., Krause, J., Niehues, J.M., Sommer, K.A., Bankhead, P., *et al.*: Pan-cancer image-based detection of clinically actionable genetic alterations. *Nature cancer* **1**(8), 789–799 (2020)
- [24] Brinker, T.J., Kiehl, L., Schmitt, M., Jutzi, T.B., Krieghoff-Henning, E.I., Krahl, D., Kutzner, H., Gholam, P., Haferkamp, S., Klode, J., *et al.*: Deep learning approach to predict sentinel lymph node status directly from routine histology of primary melanoma tumours. *European Journal of Cancer* **154**, 227–234 (2021)
- [25] Lu, M.Y., Chen, B., Williamson, D.F., Chen, R.J., Liang, I., Ding, T., Jaume, G., Odintsov, I., Le, L.P., Gerber, G., *et al.*: A visual-language foundation model for computational pathology. *Nature medicine* **30**(3), 863–874 (2024)
- [26] Su, Z., Guo, Y., Wesolowski, R., Tozbikian, G., O'Connell, N.S., Niazi, M.K.K., Gurcan, M.N.: Computational pathology for accurate prediction of breast cancer recurrence: Development and validation of a deep learning-based tool. *Modern Pathology*, 100847 (2025)
- [27] Eisemann, N., Bunk, S., Mukama, T., Baltus, H., Elsner, S.A., Gomille, T., Hecht, G., Heywang-Köbrunner, S., Rathmann, R., Siegmann-Luz, K., *et al.*: Nation-wide real-world implementation of ai for cancer detection in population-based mammography screening. *Nature medicine* **31**(3), 917–924 (2025)
- [28] Traill, M., Jantz, J., Richards, B., Khalatbari, S., Hoffmeister, J., Shisler, J., Snyder, C.: Operating point optimization for efficient mammogram triage using highly elevated artificial intelligence (ai) algorithm case and risk scores. *Clinical Breast Cancer* (2025)
- [29] Zhou, K., Yang, J., Loy, C.C., Liu, Z.: Conditional prompt learning for vision-language models. In: *Proceedings of the IEEE/CVF Conference on Computer Vision and Pattern Recognition*, pp. 16816–16825 (2022)
- [30] Zheng, Y., Gindra, R.H., Green, E.J., Burks, E.J., Betke, M., Beane, J.E., Kolachalama, V.B.: A graph-transformer for whole slide image classification. *IEEE transactions on medical imaging* **41**(11), 3003–3015 (2022)
- [31] Lin, T., Yu, Z., Hu, H., Xu, Y., Chen, C.-W.: Interventional bag multi-instance learning on whole-slide pathological images. In: *Proceedings of the IEEE/CVF Conference on Computer Vision and Pattern Recognition*, pp. 19830–19839 (2023)
- [32] Tang, W., Huang, S., Zhang, X., Zhou, F., Zhang, Y., Liu, B.: Multiple instance

learning framework with masked hard instance mining for whole slide image classification. In: Proceedings of the IEEE/CVF International Conference on Computer Vision, pp. 4078–4087 (2023)